Author(s): Kiiskinen, Titta; Mangs, Oliver; Virkajärvi, Jussi; Elsehrawy, Farid; Salo, Satu; Miettinen, Arttu; Halme, Janne; Harlin, Ali; Ketoja, Jukka A.

Title: Decontamination of a surgical mask with UV-C irradiation : analysis of experimental results with optical simulations

Year: 2024

Version: Published version

Please cite the original version:

Kiiskinen, T., Mangs, O., Virkajärvi, J., Elsehrawy, F., Salo, S., Miettinen, A., Halme, J., Harlin, A., & Ketoja, J. A. (2024). Decontamination of a surgical mask with UV-C irradiation : analysis of experimental results with optical simulations. Applied Optics, 63(25), 6523-6531. https://doi.org/10.1364/AO.528056

Research Article Vol. 63, No. 25 / 1 September 2024 / Applied Optics 6523

applied optics

Decontamination of a surgical mask with UV-C irradiation: analysis of experimental results with optical simulations

Titta Kiiskinen,[1] Oliver Mangs,[1] Jussi Virkajärvi,[1] Farid Elsehrawy,[2] Satu Salo,[1] Arttu Miettinen,[3,4] Janne Halme,[2] Ali Harlin,[1] and Jukka A. Ketoja[1,4,*]

[1] VTT Technical Research Centre of Finland Ltd, P.O. Box 1000, FI-02044 VTT, Finland
[2] Department of Applied Physics, Aalto University, P. O. Box 15100, FI-00076 Aalto, Finland
[3] Department of Physics and Nanoscience Center, University of Jyväskylä, FI-40014 Jyväskylä, Finland
[4] Department of Chemical Engineering, Mid Sweden University, SE-85170 Sundsvall, Sweden
*jukka.ketoja@vtt.fi

Received 23 April 2024; revised 8 June 2024; accepted 16 July 2024; posted 17 July 2024; published 21 August 2024

The suitability of ultraviolet-C (UV-C) irradiation for the decontamination of a surgical face mask was studied by decontamination experiments and carried out using *Staphylococcus aureus* and MS2 microbes. A moderate dosage level of 0.22 J/cm^2 achieved within 2 min led to an over 6-log$_{10}$ reduction in viable microbe contamination of the inner filtering layer. The underlying reason for this effective decontamination of fibers with small external UV-C dosage was explored with ray-tracing optical simulations, supported by optical measurements on reflection and transmission. The model 3D fiber network was constructed from X-ray tomography images of the layered mask structure consisting of polypropylene fibers. Both simulations and optical measurements indicated that UV light was able to penetrate even the deepest material regions. The simulations show that, despite radiation reflection from the outer mask layer, microbes in the actual filtering layer are affected by the radiation with increased probability due to multiple refraction and scattering of UV light from the inner fibers.

https://doi.org/10.1364/AO.528056

1. INTRODUCTION

During the last decade or so, surgical face masks [1] have become a commodity product used daily by millions of people outside the common hospital environments. The expansion in their usage has taken place mainly because of the COVID-19 pandemic [2] but also other health and environmental factors have driven this development. The large production volumes of face masks (thousands of tons daily) cause environmental and socio-economic challenges [2–4]. The non-degradable fibers (made typically of polypropylene or other plastic polymer) used in these products are a source of microplastic contaminants in water ecosystems [5,6]. On the other hand, the fluctuation in the market demand and problems in long-term storage require new solutions to assure security of supply in all situations [7].

In order to meet the above challenges, it would be important to develop systems by which the basic materials could be recycled after the mask use. One option is to disintegrate the formed material waste mechanically, chemically, or thermally and to use these fractions as raw materials for other applications, such as cementitious materials [4], polymer composites [8,9], or supercapacitors [10]. Another possibility is to re-use a face mask or some parts of it for the original purpose after effective material decontamination. Besides reducing the microplastics pollution, the advantage of this approach is that it can provide a way to tackle a temporal shortage of supplies in the market.

Several methods have been suggested for the elimination of harmful microbes, including material washing, thermal or gas treatment, chemical sterilization, and the application of ultraviolet (UV) radiation [7,11,12]. The applicability of these methods has already been proven for smooth material surfaces in common hospital environments [13]. Moreover, none of the above elimination treatments seems to change the porous structure of a surgical face mask [14], which is a basic requirement for the re-use. However, it is important to know how well the above operations decontaminate face masks that consist of several material layers with multi-scale porous structure. Decontamination can be defined in two levels: disinfection (3-log reduction) and sterilization (6-log reduction), where sterilization results in a higher reduction in the microbial count [15]. A few studies have indicated that the UV-C (wavelength 100–280 nm) decontamination of N95 filtering facepiece respirators against SARS-CoV-2 virus is possible, provided the

radiation dosage is sufficient for a given mask model [16–18]. However, a significant variation on the observed effect depending on the studied respirator part has been seen.

Our aim is to provide a fundamental understanding of experimental UV-C decontamination results for a surgical mask by X-ray structural characterization and ray-tracing optical simulations for the reconstructed microstructure. Our simulations go beyond the earlier Monte Carlo models [19,20], based on bulk optical fabric properties, or the general Kubelka's theory for layered materials [21]. The main benefit of modeling is that it provides the tools to estimate how sensitive the results would be depending on the macroscopic mask geometry, included fiber types, and used irradiation conditions. Because of light reflectance and absorption, only a part of the radiation enters the critical region of the mask. Our optical simulations based on real structural geometries enable estimating the UV radiation intensity at varied depths of the filter material. Deriving such continuous spatial information from the porous fiber network is not possible experimentally. The simulation parameters were fitted using optical measurements for its central filtering layer in the UV range before comparing the simulation results with direct decontamination experiments.

2. MATERIALS AND METHODS

A. Surgical Mask Material

The studied single-use surgical face mask (Shengquan Disposable Medical Face Mask, EN 14683:2019, Type IIR REF SMDP20603) consisted of three layers, all containing melt-blown polypropylene fibers (Fig. 1). The fibers of the middle layer had a smaller diameter than the outer layers so that the movement of microbes could be blocked with this central part (Table 1). The main role of the two other layers was to protect the filtering layer from dirt and from direct contact with large aerosol droplets. The inner layer also softens the mechanical contact with skin. Despite different fiber diameters, the layer densities were quite close to one another, as can be seen in Table 1. The fiber diameters were determined from high-resolution X-ray microtomography images (see more details in Section 2.D), utilizing the local thickness method [22].

Due to coloring and bleaching chemicals used during the manufacturing, the optical characteristics of the fibers in distinct layers could be different. Therefore, in our measurements and simulations, the middle layer was dissected and analyzed separately.

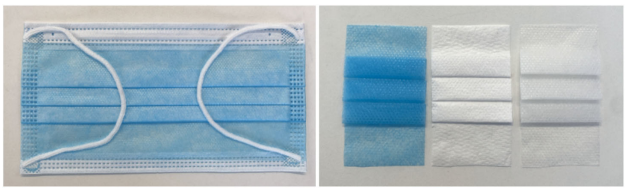

Fig. 1. Surgical mask and its three layers: the outer-colored protective layer (left), the filter layer (middle), and the skin-friendly inner layer (right).

Table 1. Properties of the Surgical Mask and Its Individual Layers[a]

Layer	Grammage g/m^2	Thickness µm	Density kg/m^3	Mean Fiber Diameter (Xradia µXCT) µm
Whole mask	83.3 ± 0.8	830 ± 20	100.4 ± 2.6	–
1 (outer)	29.7 ± 0.7	277 ± 9	107.3 ± 3.9	25.9
2 (middle)	24.6 ± 0.7	271 ± 12	91.0 ± 5.1	3.9
3 (inner)	30.1 ± 1.4	289 ± 15	104.0 ± 5.9	23.9

[a]Material thickness was measured using ProGage Thickness Tester (Thwing-Albert Instrument Company, West Berlin, NJ, USA).

B. Decontamination Experiments

The experiments were conducted in a Biosafety Level (2) laboratory at VTT Espoo, Finland. *Staphylococcus aureus* (VTT E-70045; 1.08×10^9 cfu/ml) and MS2 host *Escherichia coli* (VTT E-113164) strains were used from freeze-dried beads stored at −70 °C. A lysate was prepared from MS2 bacteriophage (DSM 13767; 1.0×10^{10} pfu/ml). The sterilization of bacteria and viruses varies based on the structure and state of the microbe [23]. Generally, viruses can be considered more resistant, but this also differs. Of the two, *S. aureus* is more susceptible to UV-C irradiation than MS2.

The standard EN 14683:2019 + AC:2019 ("Medical face masks. Requirements and test methods" annex 4 "Microbial cleanliness") was applied in the experiments. The decontamination was tested separately for the three-layer surgical mask and the middle layer. The mask was cut into 5 × 5 cm pieces and 100 µl of a microorganism solution containing *S. aureus* and MS2 was pipetted to the mask pieces as 10–20 droplets. For the full mask, the droplets were applied to the outer layer. However, this direction was not critical as the overall structure was quite symmetric (Table 1). The applied droplets remained mainly at the hydrophobic mask/layer surface both for the full mask and the separately studied middle layer. The contaminated pieces were left to dry in a laminar for 30 min in Petri dishes.

The UVC disinfection device (Biocid UVC-lamp) consisted of two low-pressure Mercury-vapor Philips UVC-lamps (Philips TUV 36T5 HO 4P SE, 253.7 nm) having the length of 30 cm. The distance from the mask piece was 10 cm. The intensity of the irradiation at the position of the tested material was measured with a UVP UVX Radiometer (Analytik Jena, Jena, Germany) connected to a UVX-25 Sensor to ensure a constant irradiance (approximately 1.8 mW/cm^2). The middle layer was irradiated from one side, and the three-layer structure was turned around halfway during the disinfection. The middle layer was irradiated for 8, 16, 27, 55, and 82 s corresponding to 0.015, 0.030, 0.050, 0.10, and 0.15 J/cm^2. The three-layer structure was irradiated for 2, 5, or 10 min corresponding to 0.22, 0.54, and 1.08 J/cm^2. After irradiation, the pieces were submerged in peptone saline containing 1% Tween. Dilution series were performed and plated onto Nutrient Agar (DifcoTM Nutrient Agar) plates and counted the following day.

C. Optical Measurements

Total hemispherical spectral reflectance R and transmittance T of the filter materials at UV wavelengths were measured

using two different spectrophotometers: Ocean Optics 2000+ equipped with a DH-2000-BAL Deuterium Halogen light source and Cary 5000 UV-Vis-NIR (Agilent, Santa Clara, CA, USA). The absorptance of the sample was calculated as $A = 100\% - R - T$. Both spectrophotometers were equipped with an integrating sphere of the type where the sample is placed outside the sphere against the sample port. These spectrophotometers use different measurement principles. The Ocean Optics 2000+ is a photodiode array spectrophotometer based on polychromatic incident light and monochromatic light detection, whereas the Cary 5000, a scanning spectrophotometer, uses the opposite configuration, namely, monochromatic incident light and polychromatic (broadband) light detection. The results from both instruments were in satisfactory agreement, which gave confidence in the validity of the results. The agreement also showed that fluorescence had no significant effect on the results [24], thus confirming that the results were suitable for comparison with the optical simulations, which did not consider fluorescence phenomena.

D. X-Ray Tomography

The fiber network structure was obtained by imaging the mask materials with two desktop microtomography scanners. The first imaging was done with Desktom 130 (RX Solutions, Chavanod, France). Pieces of 6 mm × 6 mm were cut from the mask and imaged using 40 kV X-ray tube voltage and 4 W electron beam power. The pixel size was 3.9 μm, and 1440 projection images over 360° of rotation were collected from each sample. The exposure time was 2 s, and two projection images were averaged per angular step to increase the signal-to-noise ratio. The total imaging time was, therefore, approximately 24 min per sample. The projections were reconstructed into volume images using the filtered back projection algorithm with RX Solutions XAct software and visualized using Voreen software (Fig. 2). Thresholding was applied to the volume images to create a segmentation of the fibers. The voxels in each mask image were around $4 \times 4 \times 4\ \mu m^3$, which is thus the size of the smallest observable detail described by the reconstructed structure.

From the image, it was noticed that the fibers in the middle layer of the mask were very small, having diameters (3.9 μm) around the same size as the image pixel size. To avoid possible fiber structure distortion in the image, a new cut piece from the mask was imaged with higher resolution, using the Xradia MicroXCT-400 tomography scanner (Xradia, Concord, California, USA). In this case, different material layers were carefully separated and mounted on the top of a carbon fiber sample holder rod before imaging. The X-ray source was set to 30 kV acceleration voltage and 3 W tube power. The middle layer was imaged with 0.57 μm pixel size, and the tomographic scan consisted of 2233 projection images taken over 186° of rotation with a 20 s exposure time each. The inner and outer layers were imaged with 2.2 μm pixel size, taking 941 projections over 188° of rotation with 2 s exposure time each. Three-dimensional volumetric images were reconstructed from the radiographs using the filtered back projection algorithm [25]. The area of the mask structure visible in the reconstruction was approximately 1.1 mm × 1.1 mm for the middle layer and 2.2 mm × 2.2 mm for the inner and outer layers. The reconstructed image was filtered with a bilateral filter [26]. Spatial sigma and radiometric sigma were 2 pixels and 2.5×10^{-5} for the middle layer, and 2 pixels and 1×10^{-4} for the inner and outer layers, respectively. The filtered image was thresholded with the Otsu method [27]. The remaining small background and foreground regions created from the imaging noise remaining after filtering were erased by a volume opening with a 100-pixel volume threshold [28], followed by closing the filtering with a 1-pixel radius. This final segmentation was visually checked and observed to agree with the fiber phase in the original reconstruction. Reconstruction and image segmentation were performed with the pi2 software [29,30].

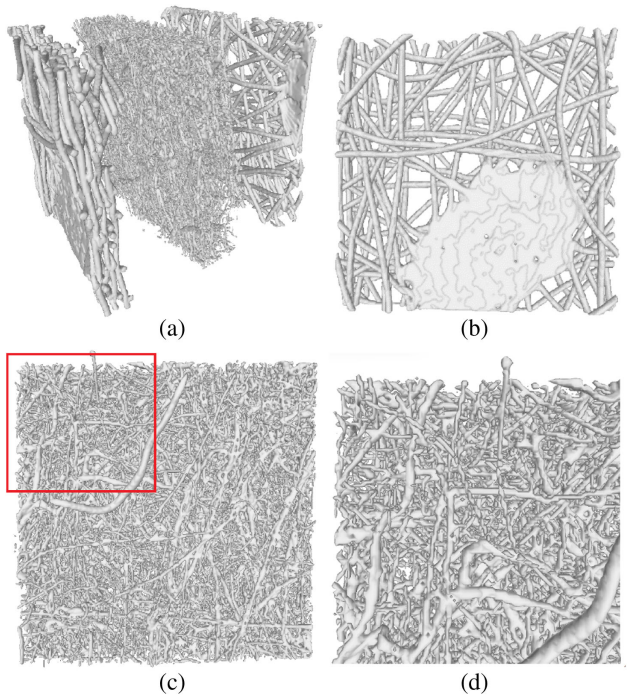

Fig. 2. (a) Desktom 130 X-ray tomography image of the surgical mask structure. (b) Outer (top) layer of the mask with melted polypropylene spots. (c) The middle layer of the size 2.174 mm × 2.617 mm. (d) Blowup of the red-boundary square of (c).

E. Building up the Simulation Geometry

To better understand the light absorption and scattering mechanisms inside the filter, we applied optical simulations to small filter volumes as described by the tomography images. This system size is sufficient to obtain information on the microscopic scattering mechanisms, and in that way assists the interpretation of the experimental decontamination results. A perfect repetition of the full macroscopic experimental setup with microscale structural features for the filter material would be impossible in the current simulations.

In order to obtain the mask fiber structure geometry in correct file format for optical simulations, the tomography images needed further processing. Slightly different processing routes were chosen for Desktom and Xradia images.

In the case of the Desktom 130 image, Fiji software [31] was used to crop it, split it into multiple sub volumes, make

it binary, and convert it, using a 3D viewer plugin, into a 3D surface mesh (*.STL). The surface mesh was then imported into MeshLab [32], where a smoothing filter called Laplacian smooth (surface preserving) was used to smooth out any odd parts left by the Fiji. The surface mesh was then imported into Fusion 360 (Autodesk, San Francisco, CA, USA), where it was repaired, converted into a solid object, and filled. Finally, the model structure was exported in ACIS format (.SAT) to the ray-tracing simulation program.

For the Xradia image, Fiji was used to scale it down by half in each dimension (using averaging and bicubic interpolation), binarize it, and crop it. The image was further symmetrically divided into eight blocks, of which two consecutive blocks, fully containing the mask middle layer in the thickness direction, were chosen for further processing. Again, the Fiji was used to generate, but also now to decimate, down to 40% of the original number of vertices, the 3D surface meshes. The two meshes were then imported to Solidworks (Dassault Systèmes, Waltham, MA, USA) as solid objects and saved in ACIS format (.SAT) for ray-trace simulations. Image scaling, cropping, division into blocks, and mesh decimation were needed for producing a manageable size (.STL) mesh file for Solidworks and (.SAT) solid object file for ray-tracing simulations.

The above image processing steps led to possible modifications in the structure. For example, the diameters of fibers may have changed slightly, and some of the fine structural details may have been merged or omitted. By comparing the simulation results obtained with both Desktom and Xradia image resolutions, the sensitivity of the results to these small changes can be estimated.

F. Ray-Tracing Simulations

The optical simulations were carried out with TracePro (Lambda Research Corp., Littleton, MA, USA), which is a Monte-Carlo-type ray-tracing software based on the classical optics theory. In the applied forward ray-tracing method (with no ray splitting), the absorption, reflection, and transmission coefficients of each object determine the probabilistic weights on how each ray progresses when it strikes the object surface [33]. The absorption profile was determined by collecting flux data at selected volume elements inside the simulated structure. The optical parameters of the model were partially taken from the literature and partially fitted based on optical measurements on the studied materials, as shall be described later.

After importing the model geometry (Section 2.E) into TracePro, it was scaled to match the actual size of the fibers and a simulation setup was built around it, in accordance with the illustration of Fig. 3. The ray source simulates the UV lamp, and the entire setup is enclosed between the two boxes so that the only way for light to pass from the left box to the right one is through the mask structure. Any rays that are absorbed in the right box have been transmitted through the sample, and any rays being absorbed in the left box have been reflected. A perfect mirror tube, guiding the light through the filter, was added to deflect light arriving at this interface back to the simulation region. This specular reflective boundary condition [34] resembles the often-used periodic boundary condition in structural and optical simulations and makes the simulations represent an infinitely large fabric sheet. This is an accurate approximation of the reality when the simulation volume is sufficiently large to represent the average properties of the sample, and the simulated optical phenomena occur at a length scale smaller than the total area of the fabric sheets. Our samples and the studied optical phenomena fulfill both conditions.

Before the actual simulations, the above procedure was validated for a 2-mm-thick solid block of polypropylene. In this case, the reflection, transmission, and absorption of light caused by the bulk material could be calculated based on Fresnel's equation and the Beer-Lambert model. The simulated results agreed with the theoretical ones up to the fourth decimal point (Fig. 4).

In the actual simulations, the simulated reflection and transmission saturated when the number of rays was at least 15,000. The simulated planar area of the Desktom mask image was 249×249 pixels, i.e., $0.97\ \text{mm} \times 0.97\ \text{mm}$, and of the Xradia mask middle layer image 150×150 pixels, i.e., $0.17\ \text{mm} \times 0.17\ \text{mm}$. The simulation time varied depending on the geometry and the number of rays, but the simulations took usually several days in a Windows 10 Pro machine equipped with an AMD Ryzen Threadripper 1950X 16-core processor running with 3.4 GHz and 128 GB RAM.

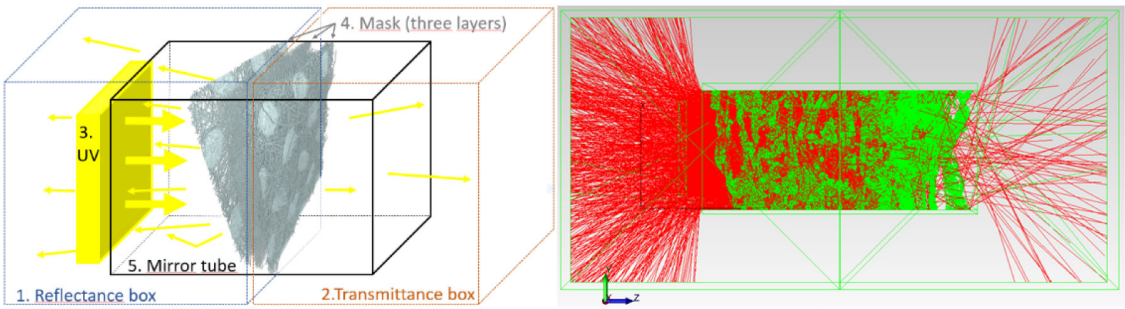

(a) (b)

Fig. 3. (a) Schematic illustration of the TracePro setup with perfect absorber boxes to obtain reflectance (1, blue) and transmittance (2, orange). The simulation box also includes the UV light source (3, yellow), the three-layer face mask structure (4, gray), and the perfect mirror square tube (5, black) that is open from the ends. (b) Sideview of a true TracePro ray-trace simulation, including reflectance and transmittance boxes, UV light source, mask middle layer, and mirror tube (all previous in green), and paths of 1000 light rays (red).

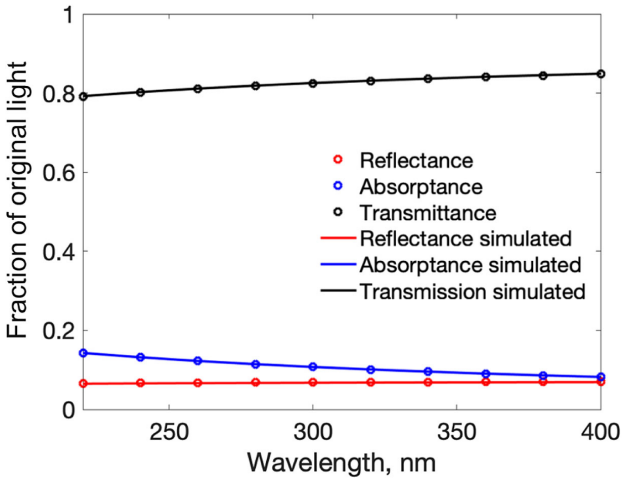

Fig. 4. Validation of the ray-tracing simulations (solid curves) against the theoretical calculation (open circles) for a solid block of polypropylene (thickness 2 mm) with refractive index $n = 1.49$ [35] and the extinction coefficient $k = 1.36 \times 10^{-6}$.

3. RESULTS

A. Optical Characterization

Figure 5(a) shows the reflectance and transmittance of the whole surgical face mask, measured with two different devices. The lower part of the spectrum, below 350 nm, is poorly transmitted and only partly reflected. Thus, the absorption can be expected to be quite high in this region of the spectrum. The outer layer of the face mask is colored, whereas the middle layer, which is not visible to the user, is less likely to contain coloring. There is an absorption peak between 260 nm and 280 nm for the middle layer, whereas above 290 nm, reflectance and transmittance are practically constant, and absorption vanishes [Fig. 5(b)].

B. Simulated Optical Properties

We took advantage of the measured optical properties of polypropylene in setting the parameters of the simulations. According to Ben Ammar and Fakhfakh [36], the refractive index of pure polypropylene increases with a decreasing wavelength. Using a UV–visible spectrophotometer, they obtained the value $n \approx 1.9$ for the refractive index at the wavelength of 250 nm. The effect of varied refractive index on simulated transmittance and reflectance for the middle mask layer turned out to be rather weak in the optical simulations. Thus, we used the value $n = 1.9$ in all mask simulations.

Ammar and Fakhfakh [36] also determined the value of the extinction coefficient k for pure polypropylene. According to their measurement, k varied in the range of $10^{-5} - 10^{-4}$ at low wavelengths, decaying rapidly around the wavelength of 280 nm. This decay made it rather difficult to determine its precise value based on the available data; therefore, we estimated the level of the extinction coefficient k by comparing the simulated optical behavior with the measured one for the middle layer. In Fig. 5(b), the measured absorption for the middle layer of the mask is around 10% at the wavelength of 280 nm, whereas the reflectance and the transmittance at this wavelength are around 65% and 25%, respectively. When using a low-resolution Desktom image in the simulations, the best fit with these values was obtained using a k-value of 4×10^{-6}, leading to the absorption of 9%, reflectance of 58%, and transmission of 33% [Fig. 6(a)]. The fairly linear behavior of the simulated absorption with penetration depth for the middle mask layer enables determining the absorption coefficient α (cm^{-1}) defined as [36]

$$\alpha = -\frac{\log_{10}(T_{\mathrm{int}})}{t}, \tag{1}$$

where T_{int} is the internal transmission of the light for the layer thickness of t. The obtained value based on simulations is $-\log_{10}(0.33/0.42)/0.28\ \mathrm{mm} \approx 0.37\ \mathrm{mm}^{-1}$. This is close to the earlier estimate obtained by Lilge *et al.* [19] for similar materials using Monte Carlo models based on bulk optical properties.

To check how the image resolution and sample geometry affected the middle-layer results, a further simulation was done with a high-resolution Xradia image [Fig. 6(b)] using the same

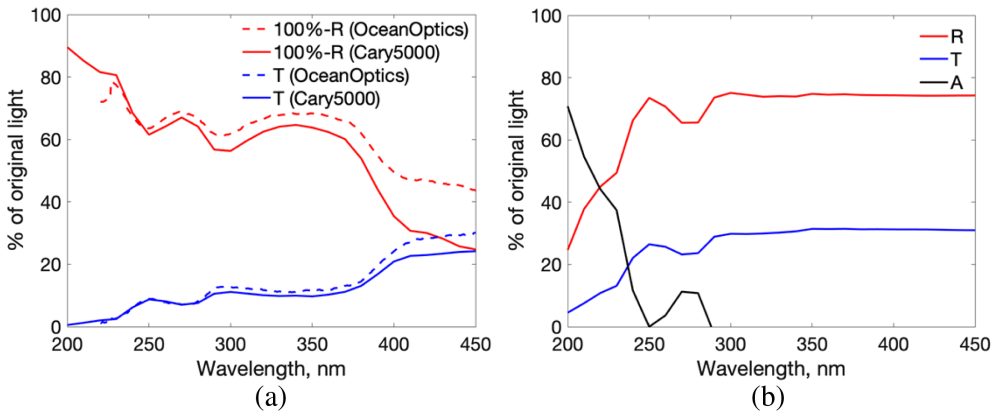

Fig. 5. Optical properties of the (a) whole surgical mask and (b) middle layer. The solid lines refer to the results obtained with the Cary 5000 instrument and the dashed lines to those obtained with Ocean Optics 2000+. In (a), the red curves show 100%-reflectance (R) and the blue curves show the transmittance (T). The absorption is obtained as $A = 100\% - R - T$, i.e., as the space between the two earlier curves. In (b), the reflectance (red curve) and transmittance (blue curve) of the middle layer become almost constant above a wavelength of 290 nm. The black curve shows the absorption of the middle layer as obtained from the measured transmittance and reflectance (possible small negative values due to experimental error in R and T measurements have been omitted).

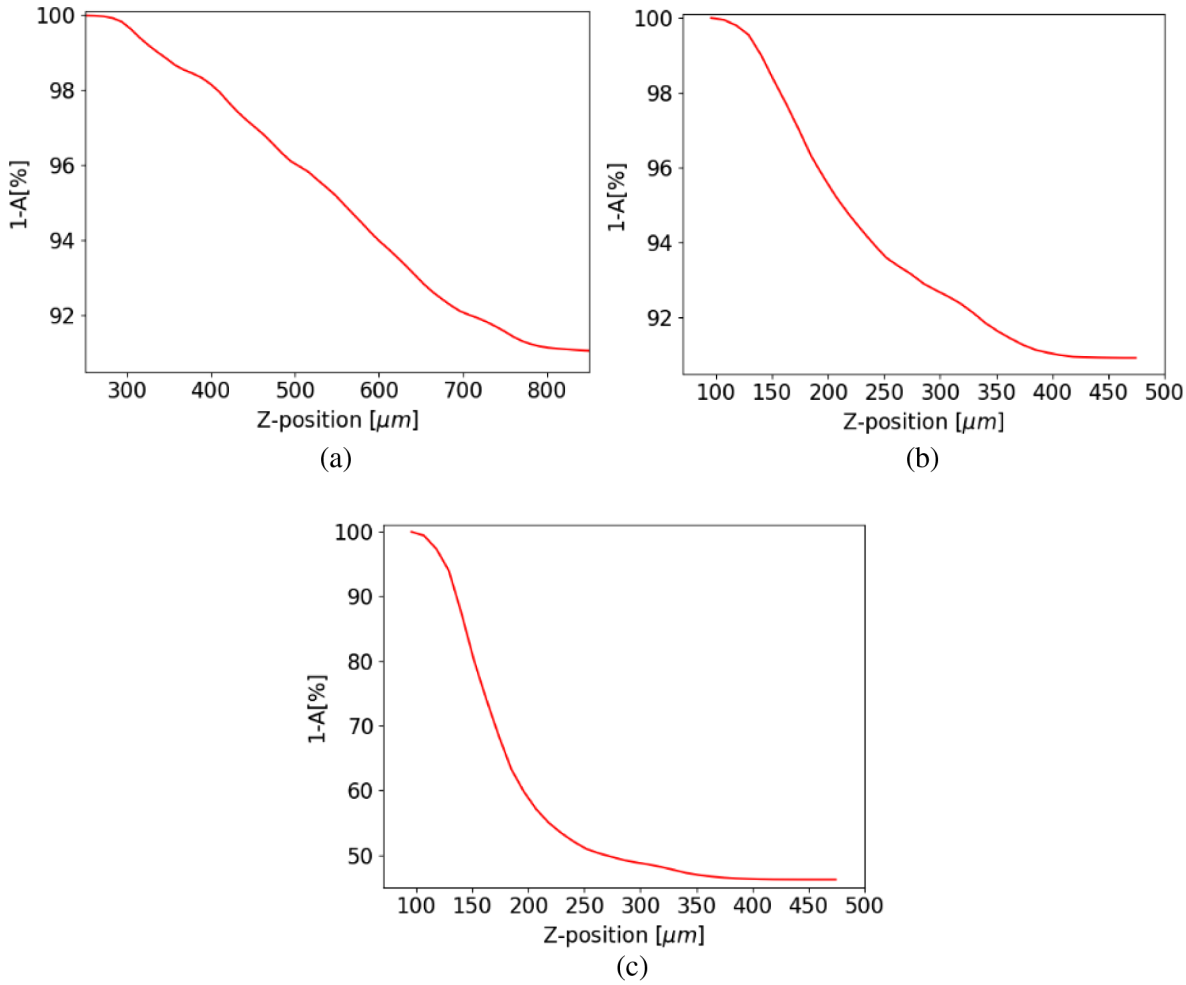

Fig. 6. Simulated attenuation of light as a function of depth for the mask middle layer based on a (a) low-resolution Desktom image, and (b), (c) a high-resolution Xradia image. The used wavelength, refractive index, and extinction coefficient values were 280 nm, $n = 1.9$, and $k = 4 \times 10^{-6}$ for (a) and (b), and 250 nm, $n = 1.88$ and $k = 8 \times 10^{-5}$ for (c).

optical parameter values (280 nm, $n = 1.9$, $k = 4 \times 10^{-6}$) as earlier. The obtained absorption, reflectance, and transmittance values were 9%, 80%, and 11%, respectively. In other words, both image resolutions led practically to equal absorption, whereas the simulated transmittance and reflectance differed between the low- and high-resolution structures, despite rather similar fiber material contents, 14% (Desktom) and 17% (Xradia), in the corresponding unprocessed images. Thus, it seems that the absorption ties to the overall solid content and to the given value of the extinction coefficient, which together determine the radiation attenuation in a solid material similarly to the Beer-Lambert law. On the other hand, the reflectance and, to some extent, also the transmittance is connected to the simulation geometry affected by the sample homogeneity, image size and resolution, and image processing.

The final simulation for the middle layer structure was done using the Xradia image with the parameters $n = 1.88$ and $k = 8 \times 10^{-5}$, as estimated for pure polypropylene, based on Figs. 5 and 6 of Ammar and Fakhfakh [36] at the 250 nm wavelength. The absorption, reflectance, and transmittance values in this case were 55%, 44.5%, and 0.5%, respectively [Fig. 6(c)]. As expected, the higher k value led to an increase in the absorption, causing reductions in the simulated reflectance and transmittance. The deviation of the simulated absorption from the measured level below 10% suggests that the optical parameters measured earlier for pure polypropylene poorly describe the radiation attenuation in a real filter material, where the fiber surfaces may have been chemically treated during processing. In particular, a lower value of the extinction coefficient than reported earlier for polypropylene [36] seems to give a much better agreement with the measured properties.

Even though a perfect agreement between the measurement for the middle layer [Fig. 5(b)] and the various simulations (Figs. 6 and 7) could not be obtained, the simulations still described quite well the measured absorption (max 10% deviation) and the transmittance (max 25% deviation) at the wavelength of 280 nm. However, we see quantitative differences between results obtained with different image resolutions and processing steps. Despite these deviations, the qualitative behavior is similar in all cases (Figs. 6 and 7). The diffuse nature of light due to multiple refraction and scattering processes inside the fiber network increases the effective radiation dosage on microbes. This is proportional to the fluence in a corresponding volume slice that includes the radiant exposure on both the

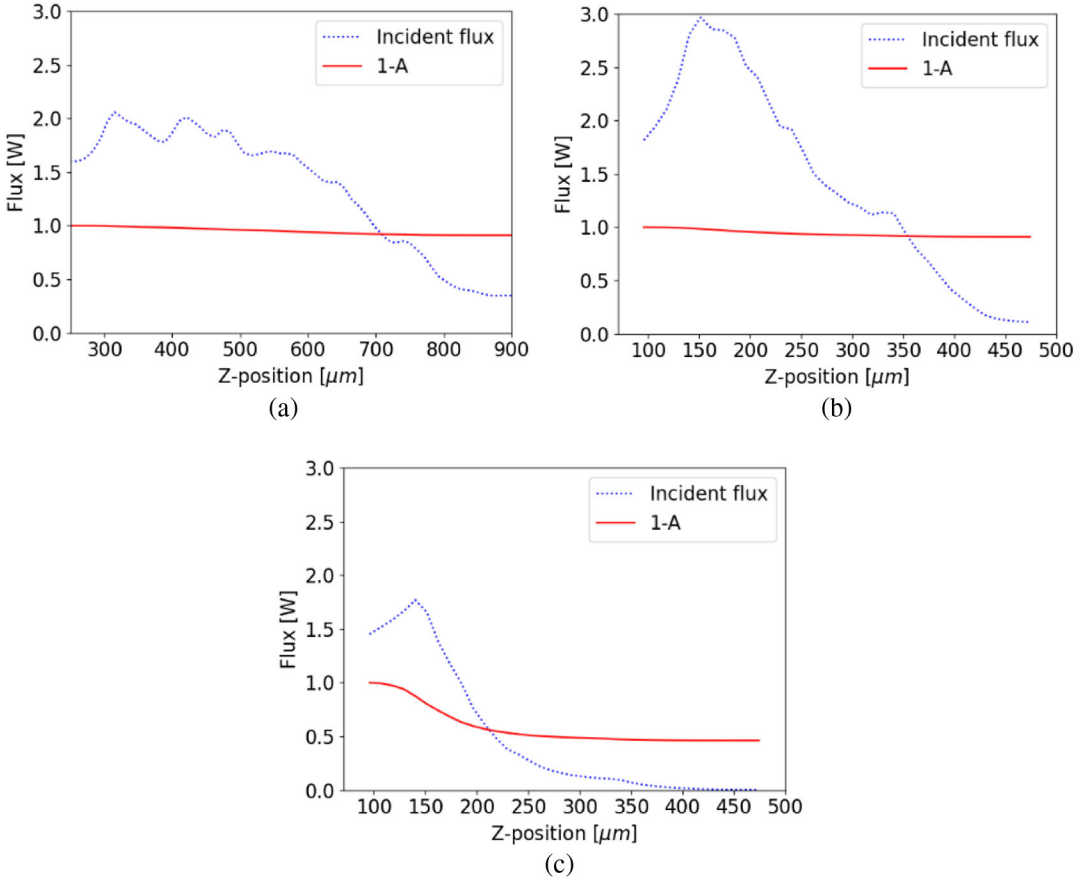

Fig. 7. Simulated incident flux (dashed blue curve) in thin (11 μm) slices of the mask middle layer at varied depth with a nominal flux of 1 W from the irradiation source. We also plot 1-A (red solid curve), where the absorption A is presented in the same units. The transmittance value can be read from the right-most point of the blue flux curve. Similarly, reflectance is the difference between the right ends of the 1-A and flux curves. The first simulations based on the (a) Desktom and (b) Xradia images were done with a wavelength of 280 nm, $n = 1.9$, and $k = 4 \times 10^{-6}$. (c) The simulation based on the Xradia image was repeated with wavelength of 250 nm, $n = 1.88$, and $k = 8 \times 10^{-5}$.

front and back slice boundary. In the TracePro simulation, this is described by the so-called incident flux, which separately accounts for all passes of a single ray into the slice. A high incident flux increases the local probability of UV-C absorption by a microbe. According to Fig. 7, the incident flux can be more than a double from the original flux from a light source. Thus, we consider this multitude refraction and scattering mechanism important for the observed strong decontamination power of UV in contaminated fiber networks, as described in Section 3.C.

For the whole mask structure, the simulations could be carried out only based on a low-resolution Desktom image because of the large system size. Using the value $k = 4 \times 10^{-6}$ for the extinction coefficient, the simulated absorption was 13% [Fig. 8(a)], i.e., clearly less than the measured level of c.a. 50% [Fig. 5(a)]. Moreover, roughly the same level of simulated absorption was obtained for the middle layer as for the outer layers, despite their very different fiber dimensions (Table 1). The simulated reflection and transmittance were 65% and 22%, respectively. The simulated transmittance was roughly twice as high as the measured one [Fig. 5(a)], and also the simulated reflectance clearly exceeded the measured one. Thus, the Desktom imaging resolution (3.9 μm) and the used simulation system size did not appear to be sufficient in describing the essential features of the full structure. The challenge was the size difference of the fibers in the middle and outer layers, together with the horizontal heterogeneity (caused by melted polypropylene) of the outer layer structure. All these factors affected the refraction and scattering processes.

C. Comparison with Measured Decontamination

Figure 9 shows the reduction of microbes during UV decontamination. The dosage achieved in 2 min, 0.22 J/cm^2, was sufficient for an over 6-log reduction for both microbes in the three-layer structure. This high decontamination efficiency could partly result from applying the radiation from both sides during the test. Lower doses of $\leq$ 0.15 J/cm^2 for the middle layer, for which the radiation was applied only from one side, resulted in 1.3–3.5-log reduction values in both microbes.

The transmission of UV radiation through a three-layer mask and the middle layer was measured using the radiometer placed underneath the sample. The distance between the UV light source and the sample was 10 cm. With the initial irradiance of 1.8 mW/cm^2 at the wavelength of 253.7 nm, the measured transmission through the three-layer structure was 0.16 mW/cm^2 and through the middle layer 0.36 mW/cm^2,

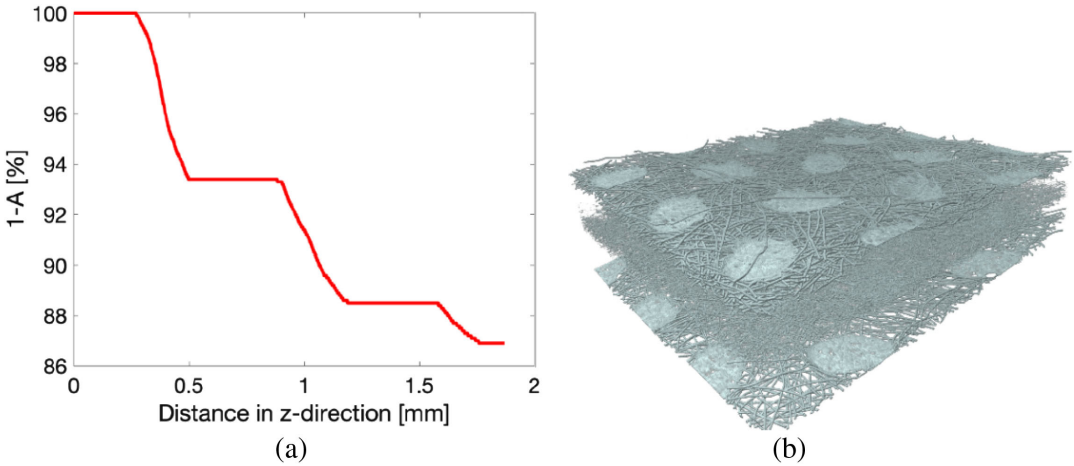

Fig. 8. (a) Simulated attenuation of light (wavelength 280 nm) as a function of depth for the whole mask structure, as described by a low-resolution Desktom image. (b) The multi-scale structural features include not only the layered structure with varying fiber dimensions but also the large-scale horizontal heterogeneity induced by the melted polypropylene regions.

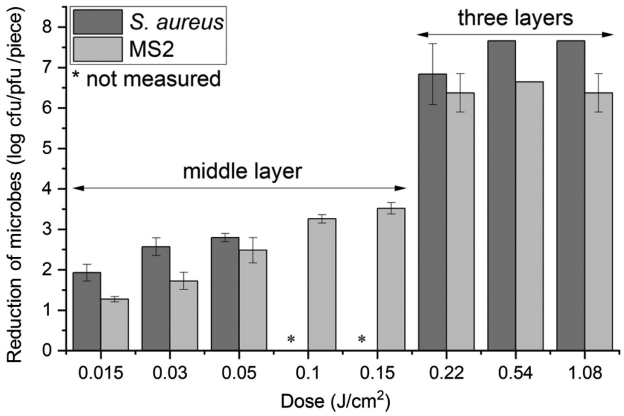

Fig. 9. Reduction of microbes during UV decontamination. Given doses and log reductions for the middle layer can be seen on the left. The piece was irradiated from the same side as the contamination had been performed. Log reductions for the higher doses on the three-layer structure can be seen on the right, where the piece was turned around halfway during the decontamination.

which were about 8.9% and 20% of the applied irradiation level. Very similar levels of optical transmission were measured at this wavelength for both structures (Fig. 5).

The comparison with the simulations is simplest in the case of middle-layer decontamination tests, in which the radiation was applied from one side only, both in the simulations and in the experiments. The simulations gave a similar transmission level, $22 \pm 11\%$ (the exact level depending on the image resolution), as experiments at a nearby 280 nm wavelength with optical parameters of $n = 1.9$ and $k = 4 \times 10^{-6}$. The corresponding absorption was only 9%, and a significant amount of the radiation got reflected. However, the internal refraction and reflection of radiation from polypropylene fibers increased the incident flux within the structure significantly as shown in Figs. 7(a) and 7(b). On average, the incident flux was at least as high as the applied level. This explains why the 3-log reduction of microbes could be observed already at a low applied radiation dose of $0.1\ \mathrm{J/cm^2}$.

For the complete three-layer structure, the turning of the mask material during the decontamination can have an effect as shown by Abdalrhman *et al.* [20]. The simulated reflectance with a lower resolution image was 65%, so that from the applied irradiance $1.8\ \mathrm{mW/cm^2}$, only about $0.6\ \mathrm{mW/cm^2}$ was absorbed or transmitted. The nominal irradiance in the middle layer was probably on a similar level. Thus, the achieved dose in 2 min, $0.22\ \mathrm{J/cm^2}$, corresponded to the incident dose of roughly $0.08\ \mathrm{J/cm^2}$ in the middle layer. This is a similar level as the one in the middle-layer tests. However, the higher 6-log reduction of *Staphylococcus aureus* and MS2 microbes for the complete three-layer structure might have resulted from the more even radiation profile due to the sample turning that prevented the formation of local low-dose regions inside the sample. Such regions are visible in Figs. 7(a) and 7(b) on the opposite side from that of the applied UV radiation. This kind of shadowing effect can be avoided by turning a sample around during the decontamination. Also, the relatively large, melted polymer regions [Figs. 2(b) and 8(b)] affect the reflectivity of the outer layers. This may increase the back and forth scattering of light inside the mask, having a positive effect for the decontamination.

4. CONCLUSIONS

The ray-tracing method seems an appropriate tool to describe the optical behavior of microporous surgical mask structure in the ultraviolet range. The simulated reflectance and transmission for the whole mask and its inner filtering layer matched reasonably well with the corresponding measured results. The advantage of the simulations is that they allow the prediction of the radiation absorption at varied depths of the filter material. This can be compared with the results of the direct decontamination experiments, allowing one to determine the level required for material purification. Even though only a part of the irradiation dosage enters the innermost filter material, the increase of a local probability of UV-C absorption by a microbe via refraction and scattering from fibers leads to an effective decontamination.

In principle, the applied methods could be used also for other types of filtering materials. However, the accuracy of the simulations depends on the resolution of the 3D imaging, which is currently limited to micrometer scale and can miss important structural features of the more efficient products like FFP masks.

Funding. Research Council of Finland (340385).

Acknowledgment. This work was supported by the Academy of Finland (Project "Citizen Shield–technological, behavioural and societal solutions for protective actions to tackle pandemics"). We are also grateful for the support from the FinnCERES Materials Bioeconomy Ecosystem.

Author contributions: decontamination experiments: TK and SS; optical simulations: OM and JV; optical measurements: FE, OM, and JH; X-ray tomography: AM; conceptualization: JH, AH, and JAK; methodology: SS, OM, JV, AM, JH, and AH; writing—original draft: JAK, OM, JV, TK, and AM. All the authors have critically revised the scientific content of this article and approved the final version.

Disclosures. The authors declare no financial or commercial conflicts of interest.

Data availability. Data that support the findings of this study are available from the corresponding author upon reasonable request.

REFERENCES

1. K. O'Dowd, K. M. Nair, P. Forouzandeh, *et al.*, "Face masks and respirators in the fight against the COVID-19 pandemic: a review of current materials," Adv. Future Perspect. Mater. **13**, 3363 (2020).
2. D. Hantoko, X. Li, A. Pariatamby, *et al.*, "Challenges and practices on waste management and disposal during COVID-19 pandemic," J. Environ. Manage. **286**, 112140 (2021).
3. E. M. Szefer, T. M. Majka, and K. Pielichowski, "Characterization and combustion behavior of single-use masks used during COVID-19 pandemic," Materials **14**, 3501 (2021).
4. M. Castellote, E. Jiménez-Relinque, M. Grande, *et al.*, "Face mask wastes as cementitious materials: a possible solution to a big concern," Materials **15**, 1371 (2022).
5. T. A. Aragaw, "Surgical face masks as a potential source for microplastic pollution in the COVID-19 scenario," Mar. Pollut. Bull. **159**, 111517 (2020).
6. O. O. Fadare and E. D. Okoff, "Covid-19 face masks: a potential source of microplastic fibers in the environment," Sci. Total Environ. **737**, 140279 (2020).
7. J. C. Rubio-Romero, M. D. C. Pardo-Ferreira, J. A. Torrecilla-García, *et al.*, "Disposable masks: disinfection and sterilization for reuse, and non-certified manufacturing, in the face of shortages during the COVID-19 pandemic," Safety Sci. **129**, 104830 (2020).
8. D. Battegazzore, F. Cravero, and A. Frache, "Is it possible to mechanical recycle the materials of the disposable filtering masks?" Polymers **12**, 2726 (2020).
9. P. J. G. Varghese, D. A. David, A. Karuth, *et al.*, "Experimental and simulation studies on nonwoven polypropylene–nitrile rubber blend: recycling of medical face masks to an engineering product," ACS Omega **7**, 4791–4803 (2022).
10. X. Hu and Z. Lin, "Transforming waste polypropylene face masks into S-doped porous carbon as the cathode electrode for supercapacitors," Ionics **27**, 2169–2179 (2021).
11. J. Militky, O. Novak, D. Kremenakova, *et al.*, "A review of impact of textile research on protective face masks," Materials **14**, 1937 (2021).
12. D. Bennet, A. F. Harris, J. Lacombe, *et al.*, "Evaluation of supercritical CO_2 sterilization efficacy for sanitizing personal protective equipment from the coronavirus SARS-CoV-2," Sci. Total Environ. **780**, 146519 (2021).
13. M. Lindblad, E. Tano, C. Lindahl, *et al.*, "Ultraviolet-C decontamination of a hospital room: amount of UV light needed," Burns **46**, 842–849 (2020).
14. E. S. Jang and C. W. Kang, "Do face masks become worthless after only one use in the COVID-19 pandemic?" Infect Chemother. **52**, 583–591 (2020).
15. T. Nicolau, N. G. Filho, J. Padrão, *et al.*, "A comprehensive analysis of the UVC LEDs' applications and decontamination capability," Materials **15**, 2854 (2022).
16. D. M. Ozog, J. Z. Sexton, S. Narla, *et al.*, "The effect of ultraviolet C radiation against different N95 respirators inoculated with SARS-CoV-2," Int. J. Infect. Dis. **100**, 224–229 (2020).
17. G. R. Golovkine, A. W. Roberts, C. Cooper, *et al.*, "Practical considerations for Ultraviolet-C radiation mediated decontamination of N95 respirator against SARS-CoV-2 virus," PLoS ONE **16**, e0258336 (2021).
18. T. Huber, O. Goldman, A. E. Epstein, *et al.*, "Principles and practice for SARS-CoV-2 decontamination of N95 masks with UV-C," Biophys. J. **120**, 2927–2942 (2021).
19. L. Lilge, A. Manalac, M. Weersink, *et al.*, "Light propagation within N95 filtered face respirators: a simulation study for UVC decontamination," J. Biophoton. **13**, e202000232 (2020).
20. A. S. Abdalrhman, C. Wang, A. Manalac, *et al.*, "Modeling the efficiency of UV at 254 nm for disinfecting the different layers within N95 respirators," J. Biophoton. **14**, e202100135 (2021).
21. R. Farnood, H. Mahmoud, J. Gibson, *et al.*, "Generalized Kubelka's theory for light transmission in multilayer materials and its application for UV light penetration in filtering facepiece respirators," J. Biophoton. **15**, e202200068 (2022).
22. T. Hildebrand and P. Rüegsegger, "A new method for the model-independent assessment of thickness in three-dimensional images," J. Microsc. **185**, 67–75 (1997).
23. W. A. M. Hijnen, E. F. Beerendonk, and G. J. Medema, "Inactivation credit of UV radiation for viruses, bacteria and protozoan (oo)cysts in water: a review," Water Res. **40**, 3 (2006).
24. A. Springsteen, "Introduction to measurement of color of fluorescent materials," Anal. Chim. Acta **380**, 183–192 (1999).
25. L. A. Feldkamp, L. C. Davis, and J. W. Kress, "Practical cone-beam algorithm," J. Opt. Soc. Am. A **1**, 612–619 (1984).
26. C. Tomasi and R. Manduchi, "Bilateral filtering for gray and color images," in *6th International Conference on Computer Vision*, Bombay, India, 1998.
27. N. Otsu, "A threshold selection method from gray-level histograms," IEEE Trans. Syst. Man Cyber. **9**, 62–66 (1979).
28. P. Soille, *Morphological Image Analysis: Principle and Applications*, 2nd ed. (Springer, 2004).
29. A. Miettinen, "pi2 program (Process Image 2)," https://github.com/arttumiettinen/pi2.
30. A. Miettinen, "Documentation and examples," https://pi2-docs.readthedocs.io/en/latest/.
31. J. Schindelin, I. Arganda-Carreras, E. Frise, *et al.*, "Fiji: an open-source platform for biological-image analysis," Nat. Methods **9**, 676–682 (2012).
32. P. Cignoni, M. Callieri, M. Corsini, *et al.*, "MeshLab: an open-source mesh processing tool," in *6th Eurographics Italian Chapter Conference*, 2008, pp. 129–136.
33. Lambda Research Corp., "User's manual for TracePro," (2022), https://www.lambdares.com/wp-content/uploads/TraceProDownload/TracePro_User_Manual.pdf.
34. J. Cai and M. F. Modest, "Specular reflective boundary conditions for discrete ordinate methods in periodic or symmetric geometries," J. Phys. Conf. Ser. **676**, 012002 (2016).
35. Scientific Polymer Products Inc., "Refractive index of polymers by index," (2021), https://scipoly.com/technical-library/refractive-index-of-polymers-by-index/.
36. L. Ben Ammar and S. Fakhfakh, "Optical and dielectric properties of polypropylene/montmorillonite nanocomposites," Funct. Compos. Struct. **2**, 045003 (2020).